Spin-dependent transport characterization in metallic lateral spin valves using one-dimensional and three-dimensional modeling

P. Laczkowski,[1,2] M. Cosset-Cheneau,[1,3] W. Savero-Torres,[1] V. T. Pham,[1] G. Zahnd,[1] H. Jaffrès,[2] N. Reyren,[2] J.-C. Rojas-Sànchez,[2] A. Marty,[1] L. Vila,[1,*] J.-M. George,[2] and J.-P. Attané[1,†]

[1]*Université Grenoble Alpes, CEA, CNRS, INP-G, IRIG, F-38054 Grenoble, France*

[2]*Unité Mixte de Physique CNRS/Thales, university Paris-Sud and Université Paris-Saclay, 91767 Palaiseau, France*

[3]*Département de Physique, Ecole Normale Supérieure de Lyon, F-69342 Lyon, France*

(Received 20 February 2019; published 24 April 2019)

We present the analysis of the spin signals obtained in NiFe based metallic lateral spin valves. We exploit the spin-dependent diffusive equations in both the conventional one-dimensional (1D) analytic modeling and in 3D finite element method simulations. These approaches are used for extracting the spin diffusion length and the effective spin polarization in Py/Al, Py/Cu, and Py/Au based lateral nanostructures at both 300 K and 77 K. Both the analytic modeling and 3D finite element method simulations give consistent results. The combination of these models provides a powerful tool for reliable spin transport characterization in all metallic spin valves and gives an insight into the spin/charge current and spin accumulations 3D distributions in these devices. We provide the necessary ingredients to develop the 3D finite element modeling of diffusive spin transport.

DOI: 10.1103/PhysRevB.99.134436

I. INTRODUCTION

Lateral spin valves (LSVs) are promising candidates for future spintronics applications, to separate spin and charge currents, and to test the first two building blocks of a spin FET device [1]: the spin injector and the spin detector. The ability to fabricate lateral devices allows one, as well, to gain in design flexibility, of both ferromagnetic and nonmagnetic elements [2]. When characterizing spin-dependent transport in LSVs, many effects need to be taken into consideration, such as the quality of the interface, the interfacial resistance, the surface of contact, and the spin flip at surfaces and interfaces, to name a few [3–7]. Moreover, one needs to take into account the possible deviation of charge current path related to either the geometry [8] or the difference in resistivities of the used materials. Three-dimensional (3D) modeling was proven to be essential for a proper analysis of the spin Hall effects [9], and therefore its development is of a great importance. So far, 1D modeling has been mainly used for the quantitative estimation of the spin-dependent transport in lateral spin valves, except in the work of Harmle *et al.* [8], where the authors used a 3D network of resistors to analyze the spin signal of Py/Cu LSVs having wide Cu channels. In this paper we present the 3D modeling of spin-dependent transport in the lateral metallic nanostructures based on the finite element method simulations, and compare it with the standard 1D analytical modeling. Our study validates the 1D approach for a fast parameter extraction in metallic and interface transparent LSVs, and provides the necessary ingredients to develop such modeling using open access software. This allows us to report consistent values of the spin diffusion length of the nonmagnetic materials and the effective spin polarization of Py in Py/Al, Py/Cu, and Py/Au based lateral spin valves at both 300 K and 77 K.

II. DEVICE PREPARATION AND EXPERIMENTAL RESULTS

In order to characterize the spin-dependent transport by extracting the spin diffusion length l_{sf}^{N} and the effective spin polarization P_{eff}, lateral spin valves (LSV) with different separation L (from center to center) of the ferromagnetic electrodes were fabricated using both the multiangle method [10] (Al and Au based samples) or the multilevel method (Cu based samples). The multilevel method consists in two sets of processes: lithography, deposit, and liftoff of the ferromagnetic (F) material, followed by the same steps for the nonmagnetic (N) material. Importantly the multilevel nanofabrication process requires the cleaning of the F/N interface by ion milling before the deposition of the nonmagnetic channel. In contrast, in the case of the multiangle evaporation technique [11–13], the sample is kept in vacuum between the F and N wire depositions and hence for the F/N interface fabrication. This ensures good contact quality, without the need of interface cleaning between the deposition of the ferromagnet and of the nonmagnetic channel.

First the 15 nm thick and 50 nm wide Permalloy stripes are deposited on the silicone substrate, followed by the deposition of the 50 nm wide nonmagnetic channel. In the case of the multiangle nanofabrication method the thickness of N is 60 nm, and in the case of the multilevel method this thickness is increased to 80 nm. Microscopic Ti(5 nm)/Au(100 nm) contact electrodes are used to connect the active part of the devices. Figure 1 represents the scanning electron microscope (SEM) images of typical nanodevices fabricated using (a) the multiangle and (b) the multilevel methods.

*laurent.vila@cea.fr

†jean-philippe.attane@cea.fr

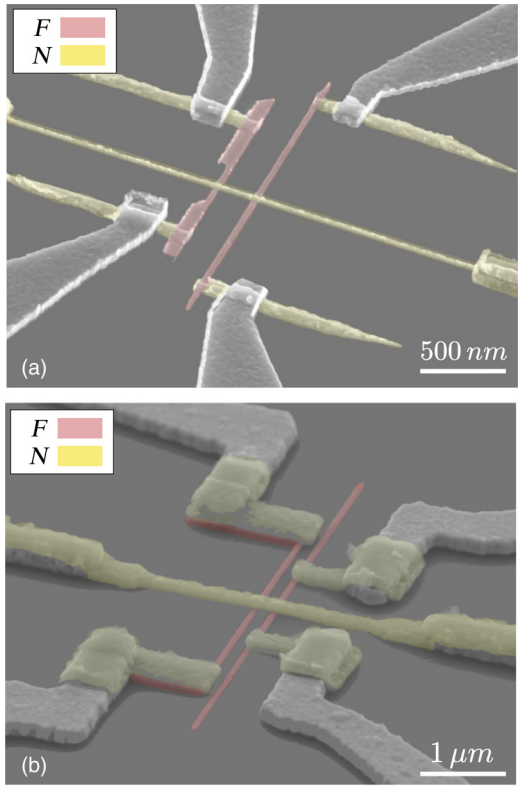

FIG. 1. SEM image of the lateral spin valve fabricated using (a) multiangle evaporation technique and (b) multilevel technique. The ferromagnetic electrodes and the nonmagnetic channel have been colored using red and yellow, respectively.

For both nanofabrication methods, in order to distinguish the switching fields of the ferromagnetic electrodes (injector and detector), we added a nucleation pad to one of the ferromagnets. This eases the nucleation process of the electrode, allowing the switching of its magnetization direction at a lower magnetic field [10].

The spin signal amplitude has been measured as a function of the distance L, varying from 100 nm to 1 μm for samples with Al, Cu, and Au nonmagnetic channels, at both 300 K and 77 K. For these three types of LSVs, a standard lock-in amplifier measurement technique has been used with 79 Hz and 100 μA ac current to measure the in-phase component of the voltage output with a magnetic field oriented along the ferromagnetic wires. The charge current injection and the voltage detection have been performed on the same side of the nonmagnetic channel using the nonlocal technique depicted in Fig. 2(a). The values of the spin signal amplitudes, ΔR_s being the change of measured voltage divided by the injected current, are reported in Fig. 2. This allows us to vary both the distance and the spin signals by at least one order of magnitude. We measured nonlocal spin signal ranging from 0.3 mΩ for Py/Au to 24 mΩ for Py/Cu based devices (Fig. 2).

III. EXTRACTION OF CHARACTERISTIC TRANSPORT PARAMETERS FROM 1D MODEL

The spin diffusion length (l_{sf}^N) and the effective permalloy stripes polarization (P_{eff}) are obtained by studying the

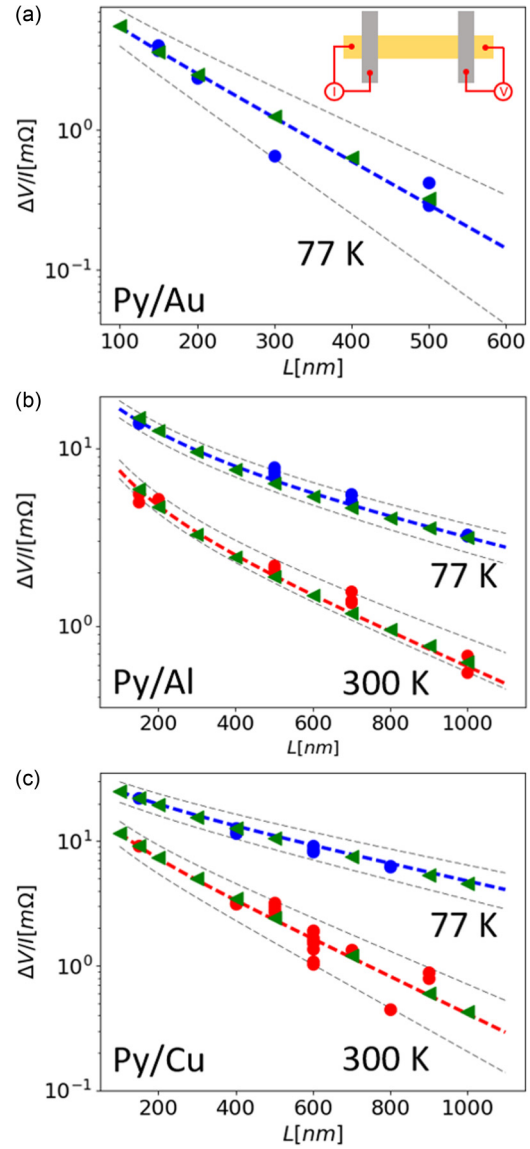

FIG. 2. Experimental data points as a function of distance L for 77 K (blue dots), altogether with the fit results using the 1D model described by Eq. (1) (dashed curves) and the FEM simulation results (green triangles) for (a) Py/Au, (b) Py/Al, and (c) Py/Cu based nanostructures. The dark dashed lines correspond to the spin signals obtained with the uncertainties given in Table I for the corresponding material combinations. The inset in (a) corresponds to the nonlocal measurement configuration, the nonmagnetic wire in yellow, and the ferromagnetic electrodes in gray.

gap dependence of the spin signal. Assuming transparent interfaces between the nonmagnetic channel and the ferromagnetic electrodes, the spin signal ΔR_s is expressed by a 1D spin diffusion model as [14]

$$\Delta R_s = \frac{4R_N(P_{\text{eff}}R_F)^2}{(R_N+2R_F)^2 e^{L/l_{sf}^N} - R_N^2 e^{-L/l_{sf}^N}}. \quad (1)$$

Here $R_{N(F)} = \rho_{N(F)} l_{sf}^{N(F)}/A_{N(F)}(1-P_F^2)$ stands for the spin resistances, where $A_{N(F)} = W_{N(F)} \times t_{N(F)}$, $\rho_{N(F)}$, $l_{sf}^{N(F)}$, t_N, and $W_{N(F)}$ are the cross sectional area, the resistivity, the spin

TABLE I. Representation of the fit results (for a given temperature) obtained by using Eq. (1) for Py/Al, Py/Cu, and Py/Au LSV samples' data sets.

Material	P_{eff}	l_{sf}^{N} (nm)	ρ (Ω nm)	T (K)
Py/Al	0.22 ± 0.01	450 ± 90	30	300
	0.32 ± 0.01	1100 ± 300	15	77
Py/Cu	0.22 ± 0.01	300 ± 60	35	300
	0.31 ± 0.03	900 ± 80	25	77
Py/Au	0.26 ± 0.01	140 ± 30	27 ± 3	77

diffusion length, the thickness and the width. The F and N subscripts correspond to the ferromagnetic and nonmagnetic material, respectively. Note that for the devices made by the multilevel method $A_F = w_F \times w_N$, while for those made by the multiangle method, $A_F = (w_F + 2t_F) \times w_N$ to take into account the conductivity of the sides of the electrodes, with w_F, t_F the width and thickness of the electrode.

Figure 2 represents the experimental data points (dots) of the spin signal amplitude as a function of distance L and fits using 1D (red and blue dashed lines) and 3D (green triangles) models for (a) Py/Au, (b) Py/Cu, and (c) Py/Al nanostructures. The data points recorded at 300 K and 77 K are represented by red and blue colors, respectively. In the case of Py/Au based samples, only low-temperature and $L \leqslant$ 600 nm measurements were possible since the amplitudes of the spin signals at 300 K and for large L were too small to be reliably detected. The estimated resistivities for Al, Cu, and Au at room temperature are 30 Ω nm, 35 Ω nm and 35 Ω nm, and at 77 K are 15 Ω nm, 25 Ω nm and 25–30 Ω nm, respectively. The resistivity and spin diffusion length of Py are 300 ± 30 Ω nm and 5.2 ± 2 nm at room temperature and at 10 K are 220 ± 12 Ω nm and 5.8 ± 2 nm [15].

The experimental data points have been fitted with two free parameters: P_{eff} and l_{sf}^{N}. P_{eff} stands for the effective spin polarization; it is basically a reduced bulk polarization as it includes the depolarization by spin flip events at the interface: the spin memory loss. P_{eff} is then smaller than the obtained bulk polarization. The spin memory loss can have various origins: spin precession due to the magnetic stray field at rough interface, the interdiffusion between F and N materials, or paramagnetic impurities [16].

Summary of the fit results for the above mentioned sample sets using the 1D model are presented in Table I. The longest spin diffusion length l_{sf}^{N} has been extracted for Py/Al, then for Py/Cu, and the smallest l_{sf}^{N} was extracted for Py/Au based structures. The extracted parameters for Py, Al, and Cu are in good agreement with what can be found in literature for similar nanostructures[4,17–22], and we find a quite long spin diffusion length ($\approx$140 nm) for Au at low temperature.

Regarding the effective spin polarization P_{eff}, the highest value at 77 K was extracted for Py/Cu and Py/Al and the smallest one for Py/Au based devices. This means that in the case of Py/Cu and Py/Al devices, the spin injection into the nonmagnetic material is more efficient than in Py/Au at 77 K. It also appears that the spin injection efficiency is similar for Py/Al and Py/Cu at 300 K and 77 K.

IV. FINITE ELEMENTS METHOD SIMULATIONS

The FEM simulations have been performed using GMSH [23], a three-dimensional finite element mesh generator, and GetDP the finite element method (FEM) solver [24,25]. A collinear approach has been used for simplicity, which is equivalent to the case of two opposite magnetization orientations along a chosen axis. It allows us to access the situation of parallel and antiparallel alignment of the ferromagnetic electrodes. In this formulation we choose a current density j to represent a flow of spins; otherwise, it would represent the electric current density and the sign of following equations would have to be changed.

Formulation. The FEM calculations are based upon the diffusive transport equations, where the currents of carriers with up and down spins have been derived from the electrochemical potentials $\mu_{\uparrow(\downarrow)}$, with different conductivities $\sigma_\uparrow$ and $\sigma_\downarrow$. In this image the current densities can be expressed in the following form:

$$\begin{aligned} \overrightarrow{j_\uparrow} &= \sigma_\uparrow \overrightarrow{\nabla}\mu_\uparrow = \sigma \frac{1+P}{2} \overrightarrow{\nabla}\mu_\uparrow, \\ \overrightarrow{j_\downarrow} &= \sigma_\downarrow \overrightarrow{\nabla}\mu_\downarrow = \sigma \frac{1-P}{2} \overrightarrow{\nabla}\mu_\downarrow, \end{aligned} \tag{2}$$

where σ is defined as $\sigma = \sigma_\uparrow + \sigma_\downarrow$, representing the total conductivity, and P is the current polarization. The charge current conservation imposes that

$$\text{div}(\overrightarrow{j_\uparrow} + \overrightarrow{j_\downarrow}) = 0, \tag{3}$$

which can be further merged with a spin relaxation proportional to the spin accumulation in the following form:

$$\text{div}(\overrightarrow{j_\uparrow}) = -\text{div}(\overrightarrow{j_\downarrow}) = \alpha(\mu_\uparrow - \mu_\downarrow) = \frac{1-P^2}{4\rho l_{sf}^2}(\mu_\uparrow - \mu_\downarrow), \tag{4}$$

where $\rho = 1/\sigma = 1/(\sigma_\uparrow + \sigma_\downarrow)$ is the global resistivity and l_{sf} is the spin diffusion length.

By combining Eqs. (2) with (4), one recovers the well known diffusion equation [26]:

$$\triangle(\mu_\uparrow - \mu_\downarrow) = \frac{\mu_\uparrow - \mu_\downarrow}{l_{sf}^2}. \tag{5}$$

For transparent interfaces, the continuity conditions on the interfaces are imposed (continuity of the electrochemical potential), together with the normal spin current densities continuity at the interfaces. The material connecting the terminals is assumed to be long enough to have vanishing spin accumulation on the terminal side. We typically choose this length to be at least three times l_{sf} and/or three times its width. The later allows the charge current to be homogeneously spread over the section of the wire far away from the interfaces. One thus assumes the same polarization on terminal faces than in the bulk material:

$$\begin{aligned} j_{\uparrow\text{surf}} &= \frac{1+P}{2}\frac{I}{A}, \\ j_{\downarrow\text{surf}} &= \frac{1-P}{2}\frac{I}{A}. \end{aligned} \tag{6}$$

The spin-dependent transport can then be defined in terms of the charge (j_c) and spin (j_s) currents by the mean and the

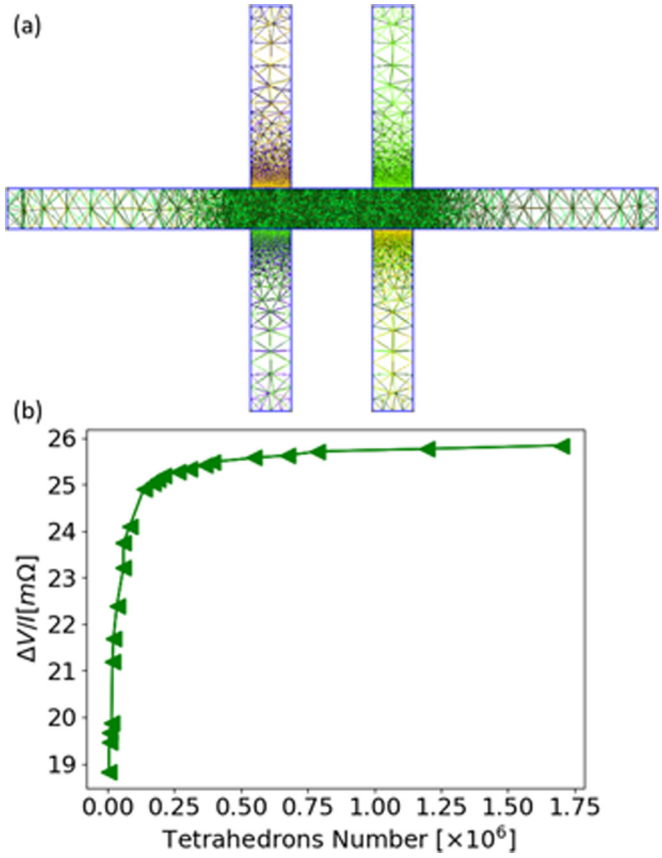

FIG. 3. (a) Mesh density used for the simulations in the lateral spin valves. The mesh density is larger in the active part (center) of the device where the right angle points and edges are concentrated. (b) Variation of the signal as a function of mesh density (expressed by the total number of tetrahedrons). The output signal corresponds to the spin signal obtained with the 3D model using the Py/Al parameters with a geometry representing a multilevel fabrication method. The spin signal depends on the mesh density for low tetrahedron number and stabilizes when the meshing is sufficiently refined. For representation purposes, the length of the metallic wires have been taken shorter than the ones used in the calculations.

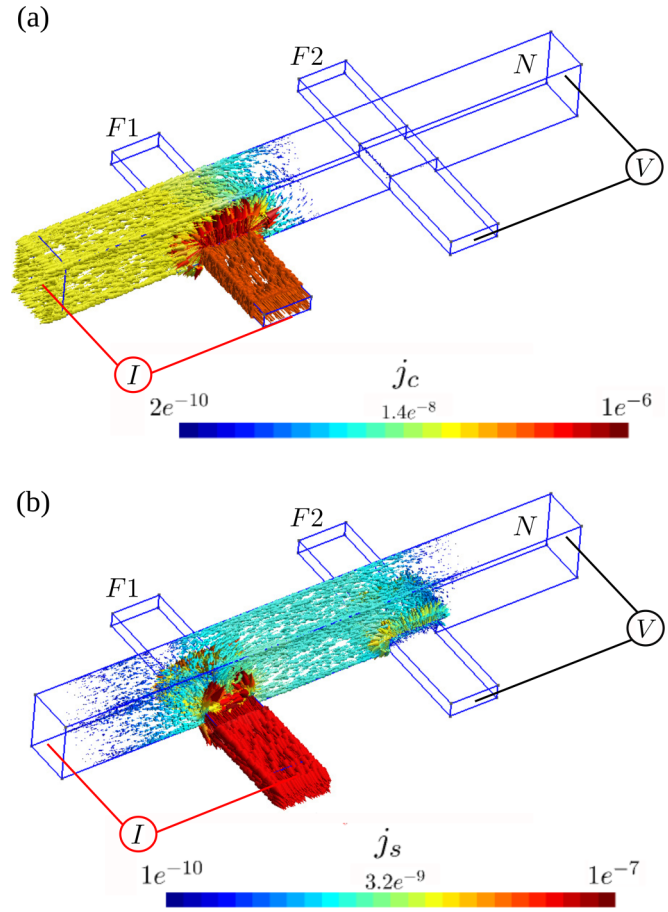

FIG. 4. FEM simulations results for a given geometry of the nanostructure with (a) charge current j_q injected at the bottom of the ferromagnetic electrode $F1$ (bottom part) and drained out through the left side of a nonmagnetic material, and (b) spin current j_s, with the efficient absorption of $F2$, reflecting the situation with $R_F < R_N$. Both j_c and j_s are displayed in the logarithmic scale.

difference of the electrochemical potentials:

$$\vec{j_c} = \vec{j_\uparrow} + \vec{j_\downarrow} = \sigma \vec{\nabla}\left(\frac{\mu_\uparrow + \mu_\downarrow}{2}\right) + P\sigma \vec{\nabla}\left(\frac{\mu_\uparrow - \mu_\downarrow}{2}\right),$$
$$\vec{j_s} = \vec{j_\uparrow} - \vec{j_\downarrow} = \sigma \vec{\nabla}\left(\frac{\mu_\uparrow - \mu_\downarrow}{2}\right) + P\sigma \vec{\nabla}\left(\frac{\mu_\uparrow + \mu_\downarrow}{2}\right). \quad (7)$$

Mesh density. The evaluation of the optimum mesh density is a very important aspect of the FEM simulations. The results of the simulations can be significantly changed when a too low tetrahedron number is used in order to mesh a given geometry. This becomes important especially in the case of geometries including right angles and edges.

In our simulations, the distance between vertices at the proximity of edges and right angles has been chosen to be 1.2 nm, which corresponds to a number of 0.5×10^6 tetrahedrons for a nonmagnetic channel of section 50 nm × 80 nm with a distance of 150 nm between the electrodes. This ensures a low variation of the output signal as shown in Fig. 3(b) when increasing the mesh density while keeping a reasonable computation time. The refined meshing area extends to a distance of 120 nm from the edges and right angles of the structure, and the distance between the vertices changes continuously to attain a value of 30 nm outside the active part of the structure [Fig. 3(a)]. We checked that the output signal does not depend on the distance between the vertices outside the active part of the structure.

Fitting using 3D model. In the 3D simulations, the distribution of the charge current, the spin current, and the spin current accumulation have been calculated for two magnetic configurations (parallel P and antiparallel AP). The spin signal amplitude has been reproduced by taking the difference of the output signals for the two states. In each case, the spin signal is evaluated from the difference of electrochemical potentials integrated on the end surface of the voltage contacts (Fig. 4). The contact wires have to be long enough (several l_{sf}) to cancel spin accumulation, so both up and down

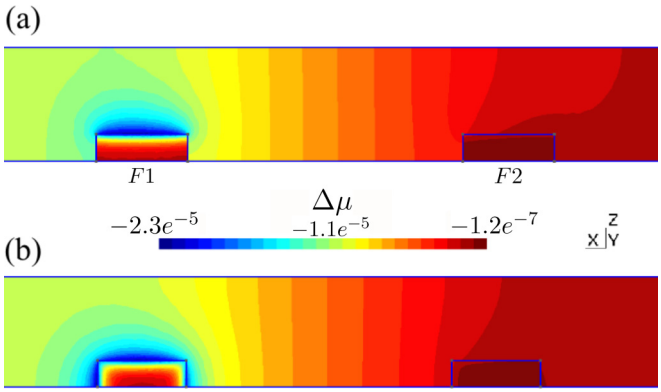

FIG. 5. FEM simulation results of the spin accumulation distribution $\mu_a = \mu_\uparrow - \mu_\downarrow$ in a LSV on the longitudinal cut at the center of N. The charge current is injected on the left side of the ferromagnetic material ($F1$), while the difference of the spin accumulation (for a given magnetic state of the system that can be parallel or antiparallel) is measured between $F2$ and the right side of N. All values are displayed by using the isosurfaces representation in the logarithmic scale.

electrochemical potentials are equal to the pure electric potential. This corresponds to the nonlocal probe configuration setup detection, where the voltage is probed between the right side of the nonmagnetic channel and the lower part of the second ferromagnetic wire.

The charge current is injected in the left side of the device through the first ferromagnetic wire and flows at the $F1/N$ interface. It is then drained out on the left side of N. This situation is represented in Fig. 4(a), where the charge current j_q is displayed using colored arrows. Thus the created spin accumulation diffuses in the nonmagnetic channel, creating the spin currents j_s. The distribution of spin currents is represented in Fig. 4(b) for the case of the AP magnetic state.

The resulting spin accumulation distribution $\mu_a = \mu_\uparrow - \mu_\downarrow$ for the AP magnetic state is represented in Figs. 5(a) and 5(b), using the ISO-surface representation. Note that two cases have been considered depending on whether the experimental data points were extracted from the multiangle or from the multilevel nanofabrication method. Figure 5(a) stands for the case where the charge current is injected into N through the top surface of the ferromagnetic electrode $F1$ which represents the multilevel nanofabrication method. Only the top surface is cleaned before the deposition of the nonmagnetic channel and the sides of $F1$ do not contribute to the current injection. Figure 5(b) represents the case describing the multiangle nanofabrication method where the active part of the device is evaporated in a single step, without breaking a vacuum, and therefore all surfaces of contact between F and N need to be taken into account in the current injection process analysis.

Table II summarizes 3D model fitting results from Fig. 2 for Py/Al, Py/Cu, and Py/Au nanostructures, assuming transparent interfaces. For all samples, the values for the effective polarization P_{eff} and spin diffusion length l_{sf}^N are only slightly larger than the ones found with the 1D model. This validates the 3D simulations and confirms the 1D approximation in our structures.

TABLE II. 3D models' fitting results of the l_{sf}^N and P_{eff} allowing one to reproduce the experimental data points.

Material	P_{eff}	l_{sf}^N (nm)	ρ (Ω nm)	T (K)
Py/Al	0.24 ± 0.01	496	30	300
	0.33 ± 0.01	1100	15	77
Py/Cu	0.24 ± 0.01	300	35	300
	0.35 ± 0.01	900	25	77
Py/Au	0.27 ± 0.01	150	30	77

V. SUMMARY FROM TWO MODELS

Parameters estimated using both above described characterization methods (1D and 3D) are summarized in Table III. Both the P_{eff} and l_{sf}^N values are in good agreement with what can be found in literature for similar nanostructures [4,27–30].

The obtained values for the effective polarization and the spin diffusion lengths obtained by 1D and 3D analysis are in good agreement. The slightly larger values obtained with the 3D model for P_{eff} may be due to the additional relaxation linked with the spatial extension of the injector. This effect is not taken into account by the 1D model that assumes a point contact between the ferromagnetic electrodes and the nonmagnetic channel [31]. This leads the 1D model to overestimate the spin signal, hence leading to a lower value for P_{eff}.

At room and low temperature the l_{sf}^N values were found to be highest for Py/Al, then for Py/Cu, and finally for Py/Au based devices. This means that at low temperatures the spin currents propagate to longer distances in Al than in Cu followed by Au channels. The effective polarization also depends on the materials combination. At low temperature, P_{eff} is larger for Py/Cu and Py/Al based devices than in the Py/Au based ones. This indicates a better spin injection efficiency for the Py/Cu and Py/Al interfaces.

VI. COMPARISON BETWEEN 1D AND 3D MODELING

We have seen in the previous section that the FEM simulations in our devices give consistent results for the materials parameters when the devices are fabricated using the multilevel method. However, the 1D model assumes a uniform

TABLE III. Summary of the fit results from 1D and 3D models, for Py/Al, Py/Cu, and Py/Au sample sets.

Material	Model	P_{eff}	l_{sf}^N (nm)	T (K)
Py/Al	1D	0.22 ± 0.01	450 ± 90	300
	3D	0.24 ± 0.01	496	
	1D	0.32 ± 0.01	1100 ± 300	77
	3D	0.33 ± 0.01	1100	
Py/Cu	1D	0.22 ± 0.01	300 ± 60	300
	3D	0.24 ± 0.01	300	
	1D	0.31 ± 0.03	900 ± 80	77
	3D	0.35 ± 0.01	900	
Py/Au	1D	0.26 ± 0.01	140 ± 30	77
	3D	0.27 ± 0.01	150	

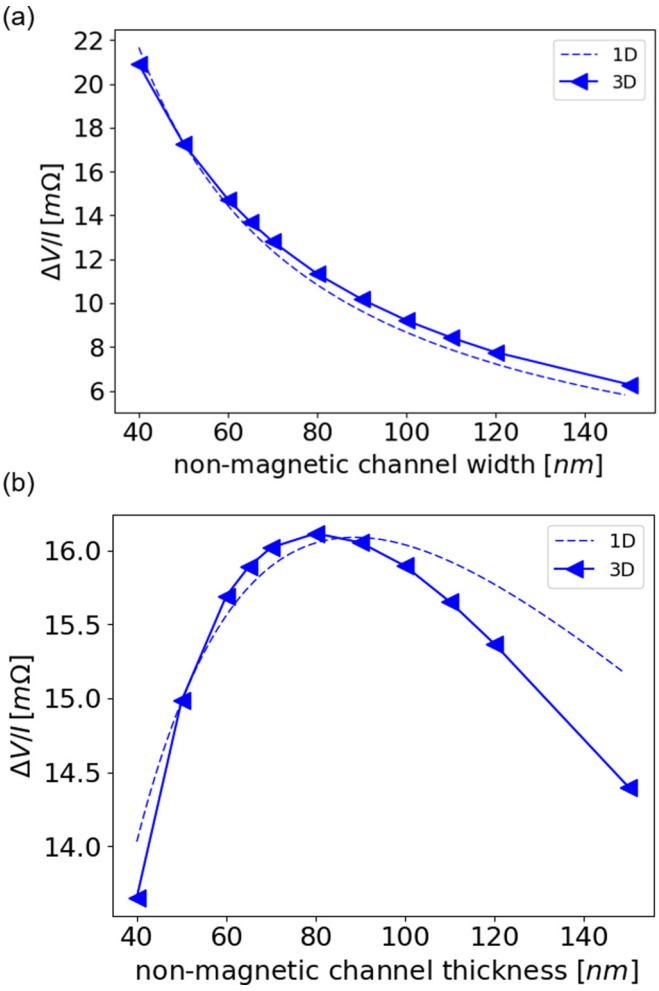

FIG. 6. Comparison of the predicted evolution of the spin signal when varying the width (a) and the thickness of the nonmagnetic channel (b) for 1D and 3D modeling. The used parameters have been obtained from 1D and 3D modeling for Py/Cu at 77 K. The measurement contacts have been taken on the same side of the device for the 3D model.

distribution of the spin current across the nonmagnetic channel section. It has been observed [32] that a variation of the nonmagnetic channel cross section can lead to a large variation of the predicted spin signal. In order to further explore the agreement of the 1D and 3D analysis, we compared the calculated spin signal obtained by the 1D and 3D model when varying the channels cross section. Increasing the width w_N [Fig. 6(a)] of the channel decreases the spin resistance of the ferromagnetic injector, resulting in a reduction of $\Delta R_s \propto 1/w_N$ according to Eq. (1) due to a lower spin injection efficiency [32]. On the other hand, an increase in the thickness t_N of the nonmagnetic channel leads to a reduction of the spin resistance mismatch, eventually leading to a better spin injection. Nevertheless, this provides more room for the spin accumulation to vanish without being detected, inducing the nonmonotonic shape observed in Fig. 6(b). This large relaxation volume effect is not taken into account by the 1D model, which explains the discrepancy with the 3D modeling for $t_N > w_N$.

We observed overall a very good agreement between the two models when varying the width of the nonmagnetic channel [Fig. 6(a)], and a good agreement with difference of less than 10% between the 1D and 3D predictions when varying the thickness of the nonmagnetic channel [Fig. 6(b)].

This validates the use of the 1D model for LSVs fabricated using the multilevel method even for large nonmagnetic channel width when its thickness is not too wide. However, for a thick nonmagnetic channel the 3D model should be used to obtain more accurate results. A precise evaluation of the spin signal change when changing the cross section of the nonmagnetic channel will be a key element for the precise evaluation of the spin diffusion length when taking into account spin-flip effects at the nonmagnetic channel surfaces [5].

VII. CONCLUSIONS

In conclusion, we have analyzed the spin-dependent transport parameters of Py based LSVs having a spin channel made of Al, Cu, and Au at $T = 77$ K and 300 K. We compared the results obtained by the conventional 1D analytical modeling of the spin transport across transparent interface to the results obtained by a 3D resolution of the problem using finite element modeling. The results of both analyses are consistent, which validates the use of 1D modeling for a fast extraction of the material parameters in the studied cases. This allows for providing quite robust material parameters l_{sf}^N and P_{eff}, of LSVs with Py electrodes and Al, Cu, and Au nonmagnetic channels, and appears to be in quite good agreement with previous experiments found in literature. The development of FEM of spin transport appears as an essential tool for further use in devices with complex geometries where 1D modeling is a too strong assumption as observed in the case of a thick nonmagnetic channel. In this paper, we provide the key ingredients required for the development of such FEM methods for studying diffusive spin transport.

ACKNOWLEDGMENTS

The devices were fabricated at RENATECH Grenoble. We acknowledge financial support from the Agence Nationale de la Recherche, Grant No. ANR-16-CE24-0017 TOPRISE and the Laboratoire d'Excellence LANEF (Grant No. ANR-10-LABX-51-01).

[1] S. Datta and B. Das, Electronic analog of the electrooptic modulator, Appl. Phys. Lett. **56**, 665 (1990).

[2] G. Zahnd, L. Vila, V. T. Pham, A. Marty, C. Beigné, C. Vergnaud, and J. P. Attané, Giant magnetoresistance in lateral metallic nanostructures for spintronic applications, Sci. Rep. **7**, 9553 (2017).

[3] L. Wang, Y. Otani, H. Idzuchi, and Y. Fukuma, Spin relaxation mechanism in silver nanowires covered with MgO protection layer, Appl. Phys. Lett. **101**, 022415 (2012).

[4] T. Kimura, T. Sato, and Y. Otani, Temperature Evolution of Spin Relaxation in a NiFe/Cu Lateral Spin Valve, Phys. Rev. Lett. **100**, 066602 (2008).

[5] M. Erekhinsky, A. Sharoni, F. Casanova, and I. Schuller, Surface enhanced spin-flip scattering in lateral spin valves, Appl. Phys. Lett. **96**, 022513 (2010).

[6] G. Mihajlovic, J. Pearson, S. D. Bader, and A. Hoffmann, Surface Spin Flip Probability of Mesoscopic Ag Wires, Phys. Rev. Lett. **104**, 237202 (2010).

[7] S. Yakata, Y. Ando, and T. Kimura, *Optimization of Interface Condition for Efficient Spin Injection in Permalloy/Cu Lateral Spin Valve*, TENCON 2010, 2010 IEEE Region 10 Conference (IEEE, New York, 2010), pp. 126–128.

[8] J. Hamrle, T. Kimura, Y. Otani, K. Tsukagoshi, and Y. Aoyagi, Current distribution inside Py/Cu lateral spin-valve devices, Phys. Rev. B **71**, 094402 (2005).

[9] Y. Niimi, Y. Kawanishi, D. H. Wei, C. Deranlot, H. X. Yang, M. Chshiev, T. Valet, A. Fert, and Y. Otani, Giant Spin Hall Effect Induced by Skew Scattering from Bismuth Impurities Inside Thin Film CuBi Alloys, Phys. Rev. Lett. **109**, 156602 (2012).

[10] P. Łączkowski, L. Vila, S. Ferry, A. Marty, J.-M. George, H. Jaffrès, A. Fert, T. Kimura, T. Yang, Y. Otani, and J.-P. Attané, Spin signal in metallic lateral spin valves made by a multiple angle evaporation technique, Appl. Phys. Express **4**, 063007 (2011).

[11] G. Mihajlovic, D. K. Schreiber, Y. Liu, J. E. Pearson, S. D. Bader, A. K. Petford-Long, and A. Hoffmann, Enhanced spin signals due to native oxide formation in $Ni_{80}Fe_{20}$/Ag lateral spin valves, Appl. Phys. Lett. **97**, 112502 (2010).

[12] S. O. Valenzuela and M. Tinkham, Direct electronic measurement of the spin Hall effect, Nature (London) **442**, 176 (2006).

[13] T. Yang, T. Kimura, and Y. Otani, Giant spin-accumulation signal and pure spin-current-induced reversible magnetization switching, Nat. Phys. **4**, 851 (2008).

[14] W. Savero Torres, A. Marty, P. Laczkowski, M. Jamet, L. Vila, and J.-P. Attané, Calculation method of spin accumulations and spin signals in nanostructures using spin resistors, Eur. Phys. J. B **91**, 37 (2018).

[15] G. Zahnd, L. Vila, V. T. Pham, M. Cosset-Cheneau, W. Lim, A. Brenac, P. Laczkowski, A. Marty, and J.-P. Attané, Spin diffusion length and polarization of ferromagnetic metals measured by the spin-absorption technique in lateral spin valves, Phys. Rev. B **98**, 174414 (2018).

[16] J.-C. Rojas-Sanchez, N. Reyren, P. Laczkowski, W. Savero, J.-P. Attané, C. Deranlot, M. Jamet, J.-M. George, L. Vila, and H. Jaffrès, Spin Pumping and Inverse Spin Hall Effect in Platinum: The Essential Role of Spin-Memory Loss at Metallic Interfaces, Phys. Rev. Lett. **112**, 106602 (2014).

[17] S. Takahashi and S. Maekawa, Spin injection and detection in magnetic nanostructures, Phys. Rev. B **67**, 052409 (2003).

[18] S. Takahashi and S. Maekawa, Spin injection and transport in magnetic nanostructures, Physica C **437-438**, 309 (2006).

[19] E. Villamor, M. Isasa, L. E. Hueso, and F. Casanova, Contribution of defects to the spin relaxation in copper nanowires, Phys. Rev. B **87**, 094417 (2013).

[20] T. Kimura and Y. Otani, Large Spin Accumulation in a Permalloy-Silver Lateral Spin Valve, Phys. Rev. Lett. **99**, 196604 (2007).

[21] P. Laczkowski, L. Vila, V.-D. Nguyen, A. Marty, J.-P. Attané, H. Jaffrès, J.-M. George, and A. Fert, Enhancement of the spin signal in permalloy/gold multiterminal nanodevices by lateral confinement, Phys. Rev. B **85**, 220404(R) (2012).

[22] T. Wakamura, K. Ohnishi, Y. Niimi, and Y. Otani, Large spin accumulation with long spin diffusion length in Cu/MgO/permalloy lateral spin valves, Appl. Phys. Express **4**, 063002 (2011).

[23] C. Geuzaine and J.-F. Remacle, Gmsh: a three-dimensional finite element mesh generator with built-in pre- and post-processing facilities, Int. J. Numer. Meth. Engng. **79**, 1309 (2009).

[24] P. Dular and C. Geuzaine, GetDP reference manual: The documentation for GetDP, a general environment for the treatment of discrete problems, http://www.geuz.org/getdp/.

[25] P. Dular, C. Geuzaine, A. Genon, and W. Legros, An evolutive software environment for teaching finite element methods in electromagnetism, IEEE Trans. Magn. **35**, 1682 (1999).

[26] T. Valet and A. Fert, Theory of the perpendicular magnetoresistance in magnetic multilayers, Phys. Rev. B **48**, 7099 (1993).

[27] M. V. Costache, M. Zaffalon, and B. J. van Wees, Spin accumulation probed in multiterminal lateral all-metallic devices, Phys. Rev. B **74**, 012412 (2006).

[28] F. J. Jedema, M. S. Nijboer, A. T. Filip, and B. J. van Wees, Spin injection and spin accumulation in all-metal mesoscopic spin valves, Phys. Rev. B **67**, 085319 (2003).

[29] Y. Ji, A. Hoffmann, J. S. Jiang, J. E. Pearson and S. D. Bader, Non-local spin injection in lateral spin valves, J. Phys. D **40**, 1280 (2007).

[30] T. Kimura, J. Hamrle, and Y. Otani, Estimation of spin-diffusion length from the magnitude of spin-current absorption: Multiterminal ferromagnetic/nonferromagnetic hybrid structures, Phys. Rev. B **72**, 014461 (2005).

[31] P. Laczkowski, H. Jaffrès, W. Savero-Torres, J.-C. Rojas-Sanchez, Y. Fu, N. Reyren, C. Deranlot, L. Notin, C. Beigné, J.-P. Attané, L. Vila, J.-M. George, and A. Marty, Evaluation of spin diffusion length of AuW alloys using spin absorption experiments in the limit of large spin-orbits interactions, Phys. Rev. B **92**, 214405 (2015).

[32] T. Kimura and Y. Otani, Spin transport in lateral ferromagnetic/nonmagnetic hybrid structures, J. Phys.: Condens. Matter **19**, 165216 (2007).